Non-line-of-sight 300 GHz band Wireless link enabled by a frequency dependent reflective surface

Frédéric Dutin, Unai Beaskoetxea Gartzia, Victor Torres, Pascal Szriftgiser, Jorge Teniente, Guillaume Ducournau

Non-line-of-sight 300 GHz band Wireless link enabled by a frequency dependent reflective surface

Frédéric Dutin, Unai Beaskoetxea Gartzia, Victor Torres, Pascal Szriftgiser, Jorge Teniente, Guillaume Ducournau *Member, IEEE*

***Abstract*—Reconfigurable Intelligent Surface is a promising technology for the up-coming sixth-generation (6G) of cellular communication networks. In this context, an experimental study of specular and nonspecular reflections of a reflective surface by scattering parameter measurements in the 300 GHz range is presented. Here we compare the insertion loss of a fixed and passive reflective surface at its optimal output deflection angle with respect to the specular reflection on a metallic plate. We propose a methodology to assess the losses induced by the surface and validate the use of the device within a THz link. At its best, around 290 GHz, the surface insertion loss is less than 3 dB compared to the metallic plate. We then investigate a non-line-of-sight THz link operating in QSPK and QAM-16 coherent transmission using the reflective surface. Data rates up to 10 Gbits/s for QSPK and 20 Gbits/s for QAM-16. This is, to the best authors knowledge, the first demonstration of a non-line-of-sight THz data-link including such reflective surface.**

***Index Terms*—Non-line-of-sight THz communications, 6G, Reflective Intelligent Surfaces (RIS), Metasurfaces, Over-the-air (OTA) scattering parameters measurements.**

I. Introduction

THE sixth generation (6G) of wireless technology promises to redefine the limits of speed, responsiveness, and connectivity and is envisioned to be available in 2030 [1]. It is then crucial for 6G to operate at frequencies close to THz range [2] which allows higher data rates in the desirable order of Terabits per second (Tbit/s), as well as ultra-low latency. In 6G, wireless connectivity will be expanded to reach Internet of Things (IoT) devices, sensors, holography-type communications and extended reality [3] but also connected and autonomous vehicles, collaborative robots and intelligent healthcare [4]. The 6G networks will also need to be integrated with AI for network management, personal user experience, and smart resource localization [5]. However, as the frequency increases, free-space pathloss represents a key challenge for long-range directive/short-range omnidirectional communications since the free-space pathloss of the THz electromagnetic signal decays proportionally with the square of the operating frequency following Friis' formula [6]. For the later, this challenge can be tackled with the use of reflective surfaces in the THz channels [7]. In addition, wave propagation at THz frequency spectrum is vulnerable to atmospheric conditions [8], [9] even though here again this can be tacked by carefully selecting the communication bandwidth to be outside of the attenuation of specific resonant frequencies, as shown in [10]. Looking beyond, making 6G features available in dense environments e.g. in cities is still a bottleneck, as all kinds of blockages can prevent the propagation of THz electromagnetic waves which traditionally rely on Line-of-Sight (LoS) communication. To date, THz communications system-level demonstrations rely on highly directive links, using simple static point-to-point scenario where the radiating antenna stays in line-of-sight with the receiver up to duplexed THz links compatible with IP protocol [11], [12]. However, with the recent approaches of join communication and sensing, as well as mobile scenarios for the communication, the THz channel is progressively entering a new phase where more complex communication scenarios are considered. The use of reflective surfaces is thus considered as a new way to enable non line-of-sight THz links, in static or dynamic (reconfiguration of the reflective surface when enabled). From this perspective, reconfigurable intelligent surface (RIS) will play a major role in establishing a direct path from transmitter to receiver. The concept of such surfaces is existing in the community since many years, named as transmit/reflect arrays or metasurfaces, before RIS term was massively used.Using such devices enables to upgrade THz usual LoS communication channels to non-LoS (NLoS) scenarios. Since RIS are expected to provide an active control the phase of an impinging THz beam, many scenarios/use cases can be enabled, paving the way towards advanced wireless communication in 6G smart cities [13]. Even if RISs have already been extensively studied from a theoretical point of view, to the best of our knowledge, only one experimental study of an active liquid crystal-based RIS [14] has been published earlier this year in the THz regime. Authors gave a method to simulate and study reflective properties of a 32×32 RIS prototype. They shown that a THz beam can be steered continuously toward a desired angle.

This work is supported by the TIMES 6G-SNS project, that received funding from the Smart Networks and Services Joint Undertaking (SNS JU) under grant agreement No. 101096307. The JU receives support from the European Union's Horizon Europe research and innovation programme. This work also received support from Contrat de Plan Etat Region (CPER) WAVETECH @HdF project and Haut de-France Regional council, IEMN UHD flagship project, the IEMN CHOP platform, and France 2030-PEPR FUNTERA and SYSTERA projects. These last projects are funded by the ANR (Agence Nationale de la Recherche) under Grants ANR-22-PEEL-0006 and 22-PEFT-0006. *(Corresponding author: guillaume.ducournau@univ-lille.fr).*

F. Dutin and G. Ducournau are with University of Lille, CNRS, Centrale Lille, Univ. Polytechnique Hauts-de-France, UMR 8520-IEMN, Institut d'Electronique de Microélectronique et de Nanotechnologie, 59000-Lille, France.

U. Beaskoetxea Gartzia and V. Torres are with Anteral, Iruña/Pamplona, Navarra, SPAIN.

P. Szriftgiser is with Univ. Lille, CNRS, Laboratoire de Physique des Lasers, Atomes et Molécules, PhLAM, UMR 8523, F-59000 Lille, France.

J. Teniente is with Public University of Navarra, UPNA, Pamplona, Navarra, SPAIN.

Manuscript received November 6, 2024; revised December 20, 2024.

Therefore, RISs are expected to be key components for 6G physical layer, enabling new features like beam management or channel estimation. However, there is a lack of experimental results to corroborate or refute these propositions towards 6G deployment: the lack of experimental proof of concept of the use of RIS to unlock intelligent programmable wireless environments [15] is a real obstacle to progress further in developing these structures, as explained in [5].

In this paper, results on free space reflection performance of a RIS are presented in the 300 GHz frequency band. At this stage, the RIS is fixed (not reconfigurable), however the proposed method and data-link validation does not required reconfigurability. Here, this work aims to study the specular and nonspecular reflections of this RIS, and compare them to the specular reflection of a reference metal plate. This enables to determine the insertion losses for the optimum angular configuration. This is a first step towards experimental study of NLoS THz paths, and how they can be enabled using these reflective surfaces. As an example, beam-steering properties of any active RIS is a fundamental subject for the development of 6G and future integrated communication and sensing (ICAS). In the paper, the RIS state-of-the-art is examined in Section II. The characterization measurements in free space with a 220-325 GHz vector network analyzer (VNA) are presented in Section III, and a THz wireless communication using the RIS, for NLoS link is presented and discussed in Section IV. The conclusions and outlook are presented in Section V.

II. RIS: CONCEPTS AND STATE-OF-THE-ART

This section discusses the concept/design, electromagnetic wave control, implementation of RISs and numerical simulations.

A. Basic concepts of RISs

The concept of RISs has been established to improve, and even enable links with reduced hardware infrastructure [16], a wide variety of wireless applications. While this technology is still ongoing in the transition from theoretical works to precise definitions, the key feature that characterizes a RIS is its dynamic response reconfigurability that can be realized with low-cost hardware [17]. Even though actual RIS technology strongly depends on the actual application and is tightly coupled to other alternative existing technologies such as active multi-antenna relays, and phased-arrays [18], theoretical [19] and algorithmic [20] works by the established community over the past years demonstrated clear advancements and valuable propositions. RIS can be applied for communication applications [21], sensing [22] as well as localization/tracking [23] and detection of passive objects [24].

B. RIS: reflective and transmitting types

Depending on the applications, different types of RIS can be used depending on their operation modes. Indeed, the first type is just signal reflection, where a RIS is conventionally used as a reconfigurable reflector, desirably steering impinging electromagnetic (EM) waves. The second type is about receiving signals (R-RIS), enabling sensing of the environment, channel state information acquisition, and localization [25]. The third type is about the signal transmission (T-RIS), when used in conjunction with signal feeding units [26], [27]. Signal reflection and reception can be used simultaneously in the H-RIS operation mode [28], which integrates the benefits of two operation modes by keeping a portion of the impinged signal power for reception and reflecting the rest. Eventually, STAR-RIS [29] combine three different operating modes 1) a portion of the impinged EM wave's power is refracted while the rest is reflected, 2) different elements switch between reflecting and refracting modes, and 3) switching in time between reflecting and refracting.

C. Control of Impinging Electromagnetic Waves

The control of impinging EM waves by RIS can be done in various ways, even if they require different hardware [15], thus enabling exciting new applications: for instance, by absorption of EM waves [28] to mitigate interference in wireless networks [29]. Other approaches rely on changing the polarization of EM waves [18] and by phase or amplitude manipulation of EM waves [30], [31]. Generally, a RIS may operate in the near or far-field (FF) regime, depending on the frequency and the RIS size. The classical far-field region refers to the region beyond the Fraunhofer distance [32], which is proportional to the square of the aperture size and inversely proportional to the wavelength of the operating frequency [33]. Other features that categorize a RIS are channel access mode, which can be half-duplex [34], or full-duplex [35] and the radiation pattern since the RIS can steer a beam across a target, shape the profile and phase of a beam or generate multiple beams for MIMO and multi-user applications.

D. Implementation

Two main approaches for RISs implementation have been mainly discussed in the literature, which are either based on traditional antenna arrays or metasurfaces. The antenna-array-based RIS [36] uses unit cells that have resonant size close to half-wavelength while the metasurface-based RISs are composed of a large number of closely spaced sub-wavelength unit cells. The operation of metasurface-based RISs is based on diffraction to split the incident EM wave into several components whose directions depend on the periodicity, operating frequency, and incident angle [37].

E. Basic operation of the proposed reflective surface

Basically, following Fig. 1(a), the reflection of an incident wave on a metal plate follows the Snell's law for which the incident angle and the reflection angle are the same, ($\theta_{\mathrm{in}} = \theta_{\mathrm{out}}$). In contrast, as shown in Fig. 1(b), reflective surface (RS) unit cells induce a phase shift of the reflected signal which does not follow the classic Snell's law anymore. Thus both angles are not equal, the difference being the phase shift gradient:

$$k_0(\sin\theta_{\mathrm{out}} - \sin\theta_{\mathrm{in}}) = \frac{d\phi_R}{dx}, \tag{1}$$

where k_0 is the wavevector of the incident signal, ϕ_R is the phase shift induced by the RS and the coordinate x is

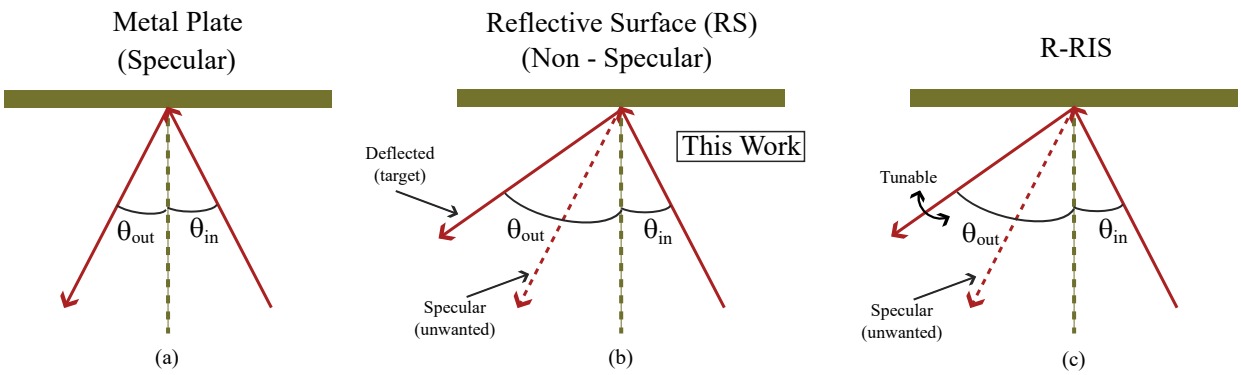

Fig. 1. (a) Metal plate operation which follows the classic reflection Snell's law ($\theta_{\text{in}} = \theta_{\text{out}}$). (b) Reflective surface (RS) operation which does not follow the classic reflection Snell's law anymore ($\theta_{\text{in}} \neq \theta_{\text{out}}$), which is the case investigated in this paper. (c) R-RIS operation where the output angle θ_{out} can be adjusted thanks to the RS reconfigurability, which is out of the scope of this paper.

tangential to the surface. (1) is known as the generalized Snell's law as described in [38]. It is worth to notice that in this configuration, the phase shift gradient is constant and is only dependent on the RS periodicity. Actually, when this phase shift gradient is not constant anymore as for R-RIS (cf. Fig 1(c)) which, for instance can be induced by Microelectromechanical Systems (MEMS) or liquid crystals, the shift between the incident angle and the reflected angle can be tuned directly.

It should be noted that while the proposed method is applied for fixed RS so far, it could be applied for reconfigurable devices, that are out of the scope of the paper.

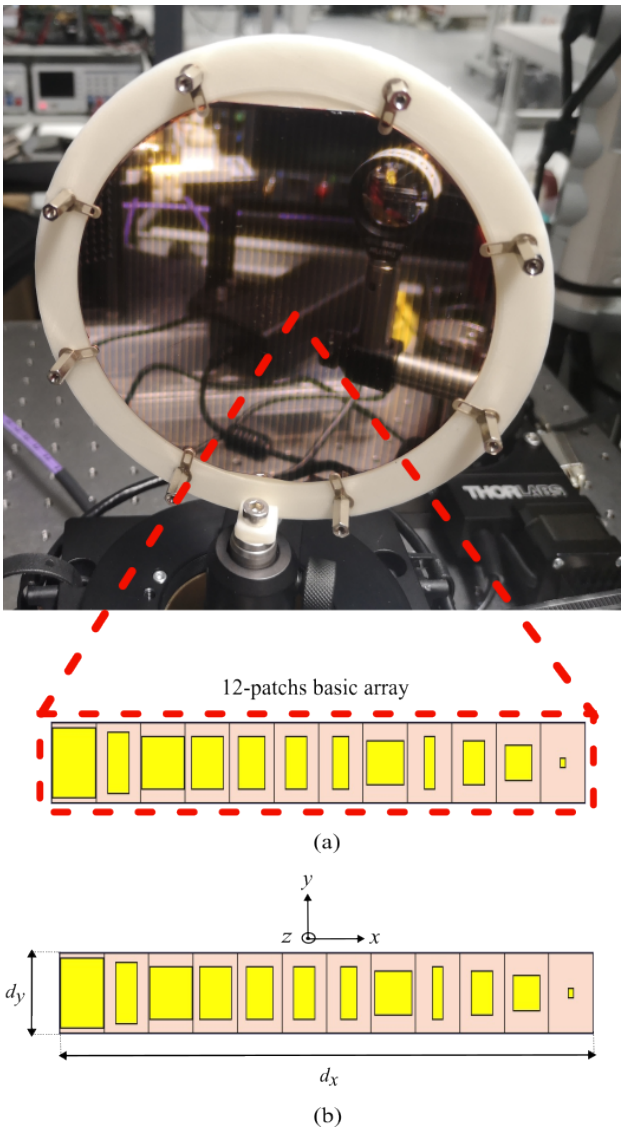

Fig. 2. (a) RS design in which the periodicity is contained on a 12-patchs basic array. (b) Schematic of a basic array with periodicity axes.

F. Reflective surface design steps

Fig. 2(a) depicts our 100 mm diameter RS fabricated on a circular wafer. The patches dimensions are obtained via simulations and optimized to produce the necessary phase change at coordinate x, according to (1). The phase shift has then been simulated for each cell that composed this RS which allows to choose a 12-patches specific configuration of a basic array. Since the patches dimensions were chosen with respect to the simulated phase shift, they do not follow any small-to-large specific distribution but they have a sub-wavelength rectangular shape with length and width from 20 $\times$ 20 µm to 160 $\times$ 160 µm. Then, the basic array is periodically repeated in both vertical and horizontal directions until the whole 4-inches wafer is covered in order to avoid parasitic reflections as shown in [39]. The periodicity is $d_x = 2.184$ mm (cf. Fig 2(b)). Moreover, because of its design, for an impinging signal with a certain polarization the RS has to be reversed oriented in order to obtain a reflected signal, i.e., if the impinging signal is horizontally polarized, the RS should be vertically oriented.

G. RS fabrication technological steps

The RS fabrication has been done at Public University of Navarra (UPNA) clean room and the basic fabrication steps are shown in Fig. 3. Here we detail these steps. Basically, an RS is a two metal layer with a top layer which is the patch array and bottom layer which is totally covered by metal. The interlayer medium is silicon. Before the photolithography process begins, the silicon wafer undergoes a cleaning procedure to ensure the removal of organic and particulate contaminants. The wafer is first rinsed with acetone, followed by a rinse with isopropyl alcohol (IPA) and spin dried afterwards. This cleaning sequence

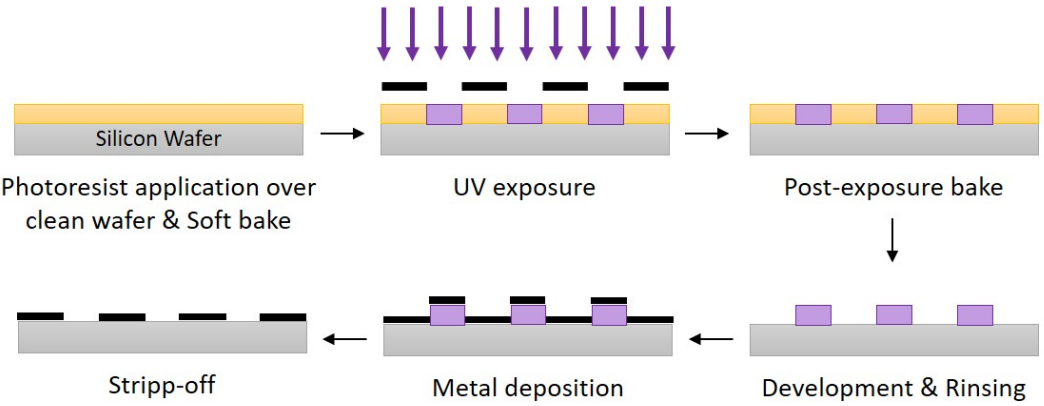

Fig. 3. Reflective Surface fabrication procedure. Metallization of the top layer with the patch array. The yellow layer is the photoresist, and the violet layer is the photoresist after the UV exposure. The black lines of last two images are the metal deposited.

ensures a clean surface for subsequent processing steps.
A uniform layer of AZ® nLOF™2020 negative photoresist is applied on a 4" circular double side polished intrinsic silicon wafer using the spin coating technique. The film thickness is set to 2.0 µm by spinning at 2500 rpm for 40 seconds. This step ensures uniform coverage of the photosensitive resin on the substrate's surface. Next, the wafer undergoes a soft bake at 110°C for 60 seconds on a direct contact hotplate. This thermal treatment evaporates residual solvents in the photoresist, improving adhesion to the substrate and optimizing the resolution of the pattern during exposure. The coated wafer is exposed to ultraviolet light at 365 nm (i-line) using a Heidelberg Instruments MLA-100 laser mask writer. The exposure energy is 66 mJ/cm^2, which enables precise transfer of the desired pattern onto the photoresist through photochemical reactions. Following exposure, a post-exposure bake is performed at 110°C for 60 seconds on a direct contact hotplate. This step is critical for stabilizing both the exposed and unexposed areas of the photoresist before development. The photolithographic pattern is developed using AZ® 326 MIF Developer in a 60-second single puddle process. The developer dissolves the areas of the photoresist that were exposed to ultraviolet light, leaving the silicon substrate's defined areas exposed. The wafer is then rinsed with deionized (DI) water to remove any developer residue and ensure the integrity of the pattern before the metal deposition process. Metal layers are deposited via electron beam evaporation (e-beam deposition). A 500 nm layer of copper (Cu) is deposited, followed by a 30 nm gold (Au) protective layer. These metal layers form the conductive parts of the reflecting surface, with the gold layer protecting the copper from oxidation. Finally, the remaining photoresist is stripped using TechniStrip® NI555, a specialized photoresist remover that efficiently eliminates the resist without damaging the deposited metal layers. This reveals the final metal circuit pattern on the silicon substrate. Again, the silicon wafer undergoes a cleaning procedure to ensure the removal of organic and particulate contaminants. The procedure is the same as in the first step. In addition to the metal deposition on the front side, a 500 nm layer of copper (Cu) followed by 30 nm of gold (Au) is also deposited on the backside of the wafer. To finish the fabrication a last cleaning procedure to ensure the removal of organic and particulate contaminants is made again. The procedure is the same as in the first step. After the complete fabrication process, the wafer is inspected using an optical microscope to verify the quality and integrity of the fabricated circuits. The inspection focuses on ensuring that the metal patterns are correctly formed, free from defects such as cracks, incomplete etching, or misalignment. This step is critical for guaranteeing the functionality of the final device before proceeding to further testing.

H. RS simulations using Floquet theory

Prior to characterization, simulations using Floquet modes [39], [40] were done in order to know the maximum non-specular reflection angles induced by the RS related to a defined incident angle, operating frequency and the periodicity of the RS. If the RS is illuminated by a plane wave, the x-component of the nth Floquet harmonic is defined as the tangential wavenumber of the reflected plane wave harmonic, k_{xn}, along the x-axis as

$$k_{xn} = k_{x0} + \frac{2n\pi}{d_x}, \tag{2}$$

where $k_{xn} = k\sin\theta_{\mathrm{Rx},n}$ and $k_{x0} = k\sin\theta_{\mathrm{Tx}}$. k is the operating wavenumber, $\theta_{\mathrm{Rx},n}$ and θ_{Tx} are the reflection angle for the nth Floquet mode and the RS's illuminating plane wave incident angle with respect to the normal of the RS, respectively. The basic array size d_x determines the ability of the RS to reflect into multiple angles depending on θ_{Tx} and $\theta_{\mathrm{Rx},n}$. The maximum reflection angle for the nth Floquet harmonic $\theta_{\mathrm{Rx},n}$ is determined by

$$\sin\theta_{\mathrm{Rx},n} = \sin\theta_{\mathrm{Tx}} + \frac{n\lambda}{d_x}, \tag{3}$$

where $\lambda = 2\pi/k$ is the operating wavelength. Because of (3), only a finite number of propagating plane wave modes significantly contribute to the field. The additional higher-order (evanescent) modes do not contribute as their propagation constants in the normal direction are imaginary. Controlling the propagating Floquet modes via the periodicity of the RS and the incident angle enables accurate prediction of reflection amplitudes, without the need for full-wave electromagnetic

simulations. The range of operating frequencies is between 220 and 325 GHz, as shown in the next section. Satisfying $|k_{xn}| < k$, there are four, five, or six propagating harmonics depending on the frequency with $n = 0, \pm1, \pm2, -3$ [41]. Specular reflections are given by the mode $n = 0$ whereas anormalous reflections are given by $n \neq 0$. Nevertheless, in our configuration, only reflection angles between 20° and 70° with respect to the normal of the RS are measured. Since they correspond to the Floquet mode $n = 1$, maximum reflection angles for each frequency of interest are thus calculated by the use of (3), with $n = 1$, as shown in Fig. 4. For θ_{Tx} less or equal to 30°, we see that the more the frequency increases, the more the reflection angle decreases. In Fig. 4, we focused on the frequency range between 270 and 320 GHz where maximum insertion losses values occur, as it will be seen later (cf. Fig. 9 and 10).

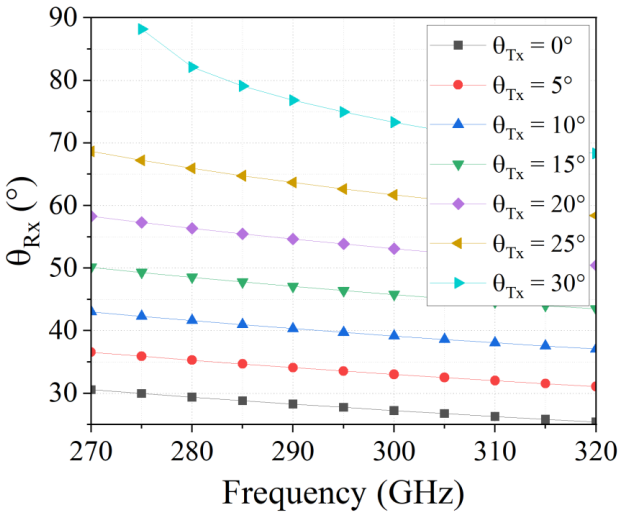

Fig. 4. Maximum reflection angles given by the Floquet mode $n = 1$ theory.

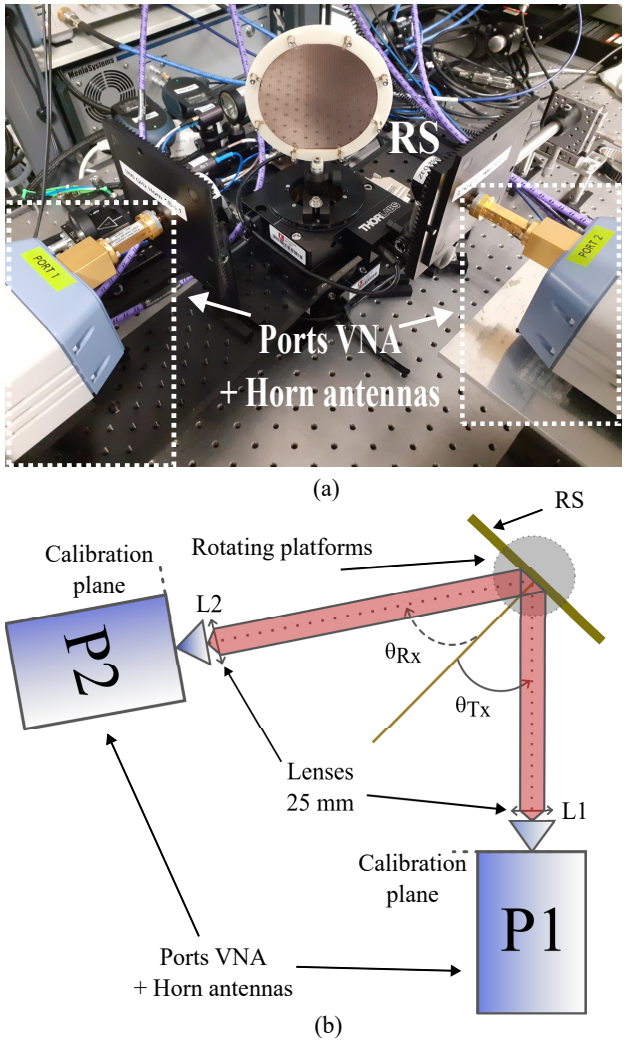

Fig. 5. (a) Photo and (b) drawing of the VNA experimental setup.

III. Characterization of the RS

This section presents the characterization measurement results. The focus is first on specular reflections and after on nonspecular reflections of the RS under test.

A. Description of the Experimental Setup

Fig. II-H(a) shows the RS during performance characterization measurements in free space with a 220-325 GHz VNA. The RS is fixed onto a first rotating platform. The incident port of the VNA is in a fixed position while the reflected port is placed on a breadboard coupled to a rotating platform. Both rotating platforms have a rotation range of 360°. With this configuration, they can be adjusted independently and we used them manually during acquisitions. To achieve the required THz alignments, both rotation stages have the same rotation axis. In the following, both sides of the RS are used. the front side is the frequency-dependent RS (cf. Fig. 2(a)), and the backside is composed of pure metal and will be used as reference. First, the VNA is calibrated using waveguide standard, with a TRM procedure (Thru, Reflect, Match) method. Doing so, the calibration plane is then set at the WR3.4 VNA outputs (cf. Fig. II-H(a)). Then, over-the-air (OTA) measurements are enabled by connecting horn antennas at both VNA outputs. The standard horns are connected on each port of the VNA and are at the same height as the center of the RS. In order to illuminate the RS with known k-vector direction, the beams are collimated by using two THz lenses. These lenses (diameter 25 mm, focal length 25 mm) are placed in front of horn antennas. The distance between horn and lens is adjusted to get the lens focal point corresponding to the phase-center of each horn antenna. The collimated beam is then illuminating the RS, deflected and collected again by the second lens (L2). The distance between the lenses and the RS is about 125 mm.

The antenna gains over the WR3.4 band were checked prior to experiment. For this, a set of identical horns are aligned and gain calculated from S_{21} and the usual Friis equation. The typical gain is shown in Fig. 6.

In Fig. II-H(b), θ_{Tx} and θ_{Rx} are the incident angle and the reflected angle with respect to the normal of the RS, respectively. Angles are adjusted using rotation stages with

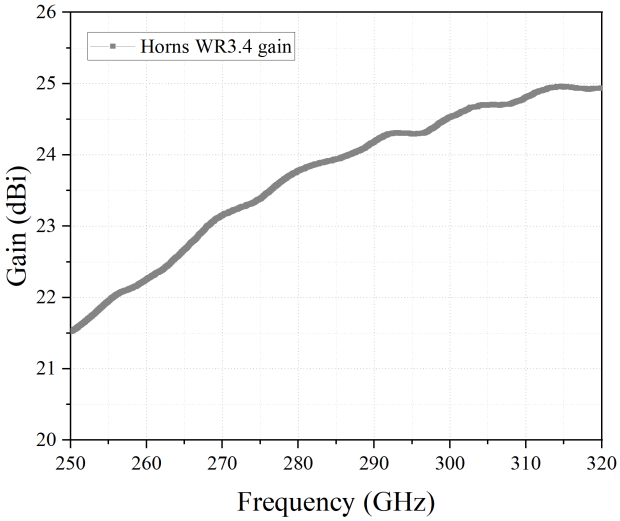

Fig. 6. Horn antenna gain (Horn input is a WR3.4 waveguide.

TABLE I
COUPLE OF ANGLES FOR INSERTION LOSS MEASUREMENTS. GRAY CELLS CORRESPOND TO SPECULAR CONFIGURATIONS.

$(\theta_{\text{Tx}}, \theta_{\text{Rx}})$					
(20,20)	(25,25)	(30,30)	(35,35)	(40,40)	(45,45)
(15,25)	(20,30)	(25,35)	(30,40)	(35,45)	(40,50)
(10,30)	(15,35)	(20,40)	(25,45)	(30,50)	(35,55)
(5,35)	(10,40)	(15,45)	(20,50)	(25,55)	(30,60)
(0,40)	(5,45)	(10,50)	(15,55)	(20,60)	(25,65)
(-5,45)	(0,50)	(5,55)	(10,60)	(15,65)	(20,70)

a 5° step (identical for θ_{Tx} and θ_{Rx}) and are swept from 0° to 45° for θ_{Tx} and from 20° to 70° for θ_{Rx}. According to the testbed configuration, the specular reflection can be measured for $\theta_{\text{Tx}} = \theta_{\text{Rx}}$ from 20° to 45°, enabling to assess the impact of the incident angle on RS's absorption bandwidth discussed in the next section. Then we measured the S_{21} parameter for all different angles couples $(\theta_{\text{Tx}}, \theta_{\text{Rx}})$ which are noted in Table I. Gray cells correspond to specular configurations, where $\theta_{\text{Tx}} = \theta_{\text{Rx}}$. As shown in Table I, we did 36 measurements for the RS but also for the metallic backside of the RS for reference. Knowing $(\theta_{\text{Tx}}, \theta_{\text{Rx}})$, we could acquire all the data. For each value of θ_{Rx}, we rotated the RS to change θ_{Tx} and acquired the S_{21} amplitude and phase.

B. RS Bandwidth Analysis using Specular Response Analysis

First, we compared S_{21} amplitudes of specular reflections for the RS and for the metallic plate (RS back-side) for different incident angles. Before any interpretations, as seen in Figs. III-A(a)-(f) and 9(a)-(e) the curves we measured were particularly affected by standing wave due the quasi-optic configuration rather than induced by the RS. Thus, we smoothed all of them by using a Savitzky-Golay filter of degree 3 where the span is about 20 points for a 5 GHz spectral range to obtain Fig. 8(a)-(f) and 10(a)-(e). In Figs. 8(a)-(f), we note that in the specular case, the metal plate and the RS got almost the same S_{21}. Thus, the RS is not absorbing anything between 220-270 GHz and 315-325 GHz (mirror-like behavior). Nevertheless, from 270 GHz to 315 GHz, for each incident angle, we have a clear absorbing behavior with a decreased S_{21} up to an 15 dB absorption level. However, the incident angle seems to play a role related to the range of absorbed frequency (AF) range. In the proposed method, the determination of the RS absorbing frequency range in the specular case provides the basis of the next analysis which focus on the nonspecular behavior of the RS. Indeed, the RS nonspecular operation frequency bandwidth should correspond to the RS specular absorption band, which is to be determined prior to the nonspecular analysis.

C. Frequency band of the RS in the Nonspecular case

The nonspecular S_{21} curves displayed in Fig. 10(a)-(e) which enable to compare RS nonspecular reflections with the metal plate specular reflection. About these nonspecular reflections, two distinct patterns occur. A "quasi-specular reflection" is observed when θ_{Tx} and θ_{Rx} are close to each other (about 10°) and a clear nonspecular reflection when angles are further from each other. Outside the RS bandwidth (270-315 GHz), a 40 dB decrease occurs for $\theta_{\text{Tx}} = 20^\circ$ between 220 and 260 GHz. In the RS bandwidth, the amplitude of the S_{21} is progressively increasing with incident angle, reaching its maximum of about -20 dB for angles $(\theta_{\text{Tx}}, \theta_{\text{Rx}}) = (60^\circ, 20^\circ)$. It confirms the RS bandwidth determined in the specular experiments.

In addition, we can clearly see the effect of moving the Rx antenna with respect to the RS. For instance, for $\theta_{\text{Tx}} = 20^\circ$, when θ_{Rx} increases we first observe a decrease of S_{21} magnitude (red and blue curves) then an increase (green and violet curves) and eventually a decrease (orange curve). Thus, in nonspecular case, we have, for each θ_{Tx}, a maximum of S_{21} for one θ_{Rx} when the angular configuration is optimal, corresponding to the optimal non-specular reflection on the RS. When the angular configuration is not optimal, a lower S_{21} is observed, which corresponds to a sub-optimal reflection case. We also observe in Fig. 10(a) and 10(b) that for incident angles larger or equal than 15° and less than 30° we have a 40° shift between specular and nonspecular reflections. Besides the quasi-specular reflection which always follows the specular one, we usually have a minimum at roughly $\theta_{\text{Rx}} = 40^\circ$ and a maximum 20° more. Also, when comparing with Fig. 4, maximum reflection angles are close to the simulated one with Floquet theory.

D. Determination of the RS losses

As displayed in Fig. 11, we zoomed on the measured S_{21} specular reflection obtained with the metallic plate (RS back-side) and the highest level obtained for nonspecular reflection from the RS was reached for angles $(\theta_{\text{Tx}}, \theta_{\text{Rx}}) = (20^\circ, 60^\circ)$ between 280 and 300 GHz. The minimum loss induced by the RS is then the relative amplitude shift between the two S_{21} curves. It is found that, related to the metal plate, the lowest RS loss is about 3 dB and occurs at about 290.6 GHz. The total RS bandwidth (@3dB) is found to be about 10 GHz. However, when using the RS inside a THz data-link with a wideband signal (modulated THz data), the overall loss

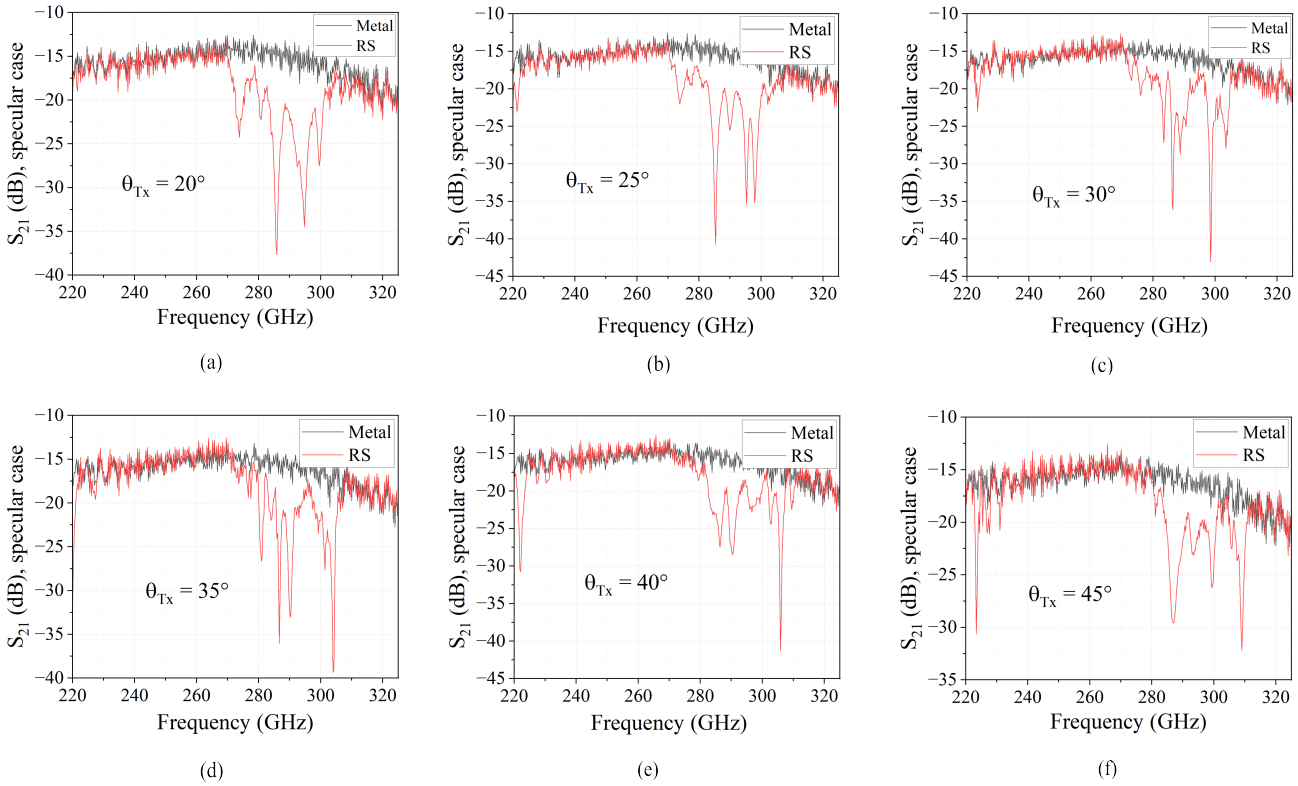

Fig. 7. Non-smoothed S_{21} amplitudes for specular reflection ($\theta_{\text{Tx}} = \theta_{\text{Rx}}$) configuration for the RS (red) and for the backside metallic plate (black) for (a) $\theta_{\text{Tx}} = 20°$, (b) $25°$, (c) $30°$, (d) $35°$, (e) $40°$ and (f) $45°$.

induced by the RS corresponds to the averaged S_{21} over the signal bandwidth, that is close to 5 GHz (see section IV). Considering the modulated spectrum in Fig. 11 lead to a loss of about 4 dB. In the next part, this angular configuration (minimum RS loss) serves as a basis for the use of the RS inserted in a THz wireless link, described in the next section.

IV. Terahertz Communication Link Confirmation

This section presents the use of the RS integrated in a THz data link. To do so, a THz link, composed of a photonic-based transmitter combined with an electronic receiver (down-converter) is used and it is shown that the link is porperly working. The measured power penalty induced by the RS in the THz path is close to the RS reflection loss measured in the VNA OTA experiment, validating the insertion of the RS within a real THz link.

A. THz link Setup

To enable the test of the THz data link, the 2 VNA heads of Fig. II-H(b) are replaced by a modulated signal source used instead of VNA port 1 (P1 in Fig. II-H(b)), and the receiver circuits are placed in place of the VNA port 2 (P2). A schematic diagram of the transmit and receive units is given in Fig. 12. Here, the photomixing concept is used to generate THz modulated signals, leveraging the techniques widely used in fiber-optic communications. The transmitter is using two continuous wave (CW) lasers, one is modulated, and the other one is CW. The optically modulated one is obtained using I and Q baseband signals to drive an optical IQ Mach-Zehnder modulator (MZM). This results in an optical quadrature phase shift keying (QPSK) or quadrature amplitude modulation with 16 states (QAM-16). The baud-rate used is fixed and set to 5 GBaud considering the RS available bandwidth. The fiber output of the MZM is combined with the CW laser which acts as a local oscillator. The lasers are free-running, with an intrinsic instantaneous linewidth of 10 kHz. This optical is amplified thanks to an erbium doped fiber amplifier (EDFA), to further feed the waveguide output UTC-PD, connected to the WR3.4 horn antenna. Using a 292 GHz detuning of the lasers enables to generate a 292 GHz signal at photomixer output.

It should be noted that the 292 GHz frequency was chosen to get optimum performances considering the testing system (transmit/receive system in back to back mode).

The signal is then propagated in the over-the-air (OTA) case, using the same THz configuration than the one used for RS measurements (Fig. II-H(b)). At the receiver side, the 292 GHz is down-converted using an electrically pumped subharmonic mixer (SHM) (WR2.8 model from VDI [42]) allowing the modulated THz signal to be down-converted into an intermediate frequency (IF) <40 GHz. The roll-off effect

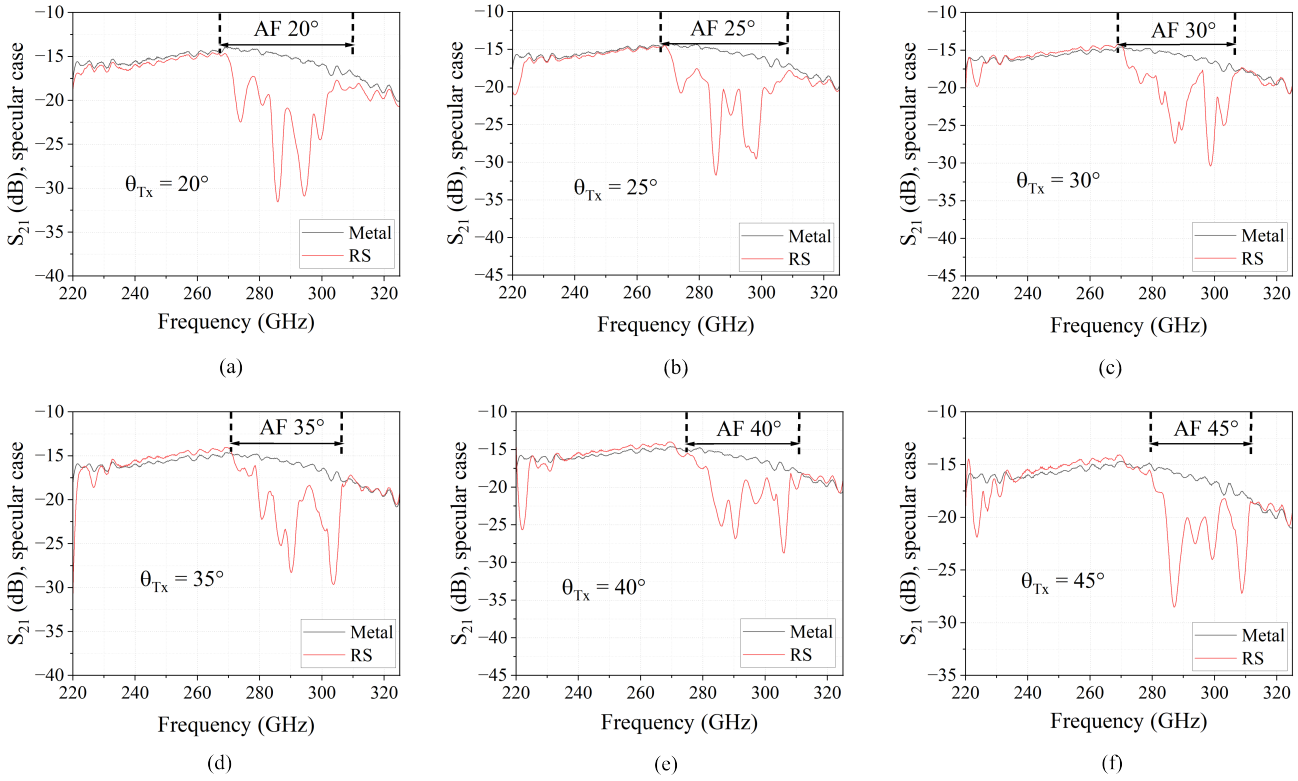

Fig. 8. Smoothed S_{21} amplitudes for specular reflection ($\theta_{\mathrm{Tx}} = \theta_{\mathrm{Rx}}$) configuration for the RS (red) and for the backside metallic plate (black) for (a) $\theta_{\mathrm{Tx}} = 20°$, (b) 25°, (c) 30°, (d) 35°, (e) 40° and (f) 45°. The identified absorbed frequencies (AF) bandwidths in this figure show the frequency region where the RS is absorbing in the specular case.

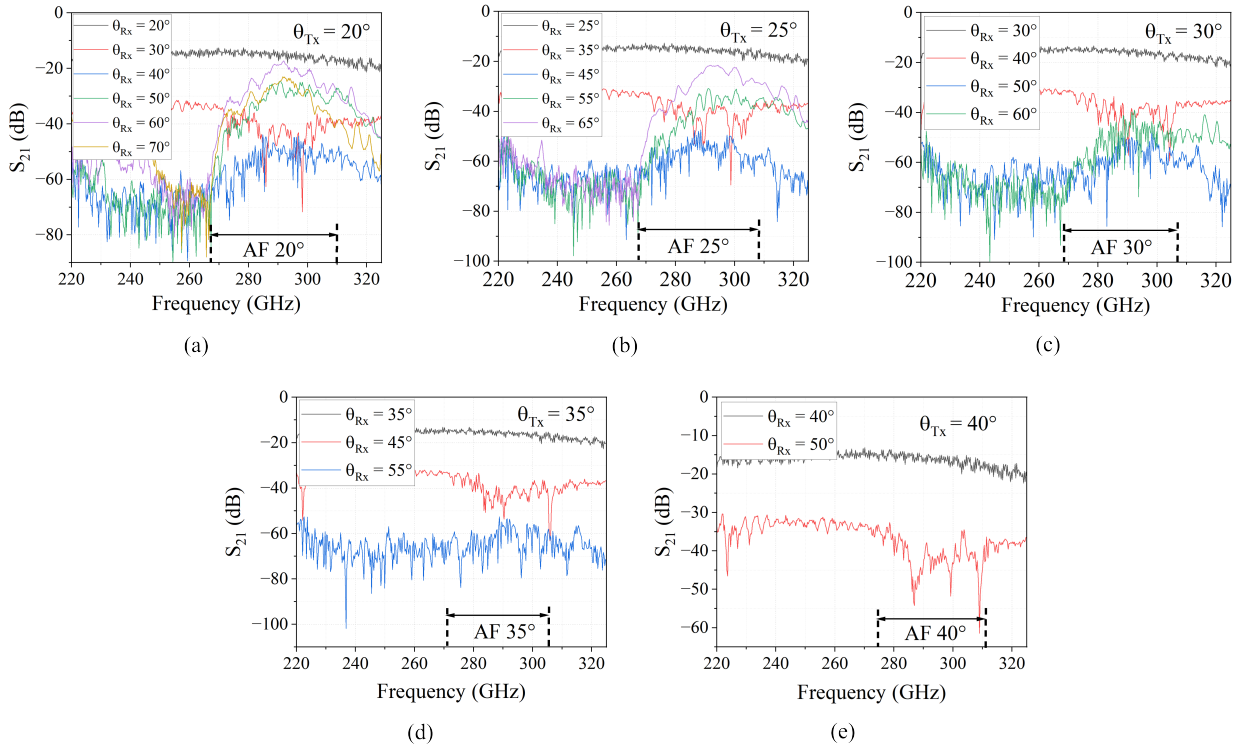

Fig. 9. Comparison between non-smoothed S_{21} for a metallic plate specular reflection (black) and nonspecular reflections from a RS (other colors) for (a) $\theta_{\mathrm{Tx}} = 20°$, (b) 25°, (c) 30°, (d) 35° and (e) 40°. The indicated bandwidth corresponds to the absorbed frequency (AF) range in the specular mode, see Fig. 8, this frequency being then non-specularly radiated from the RS.

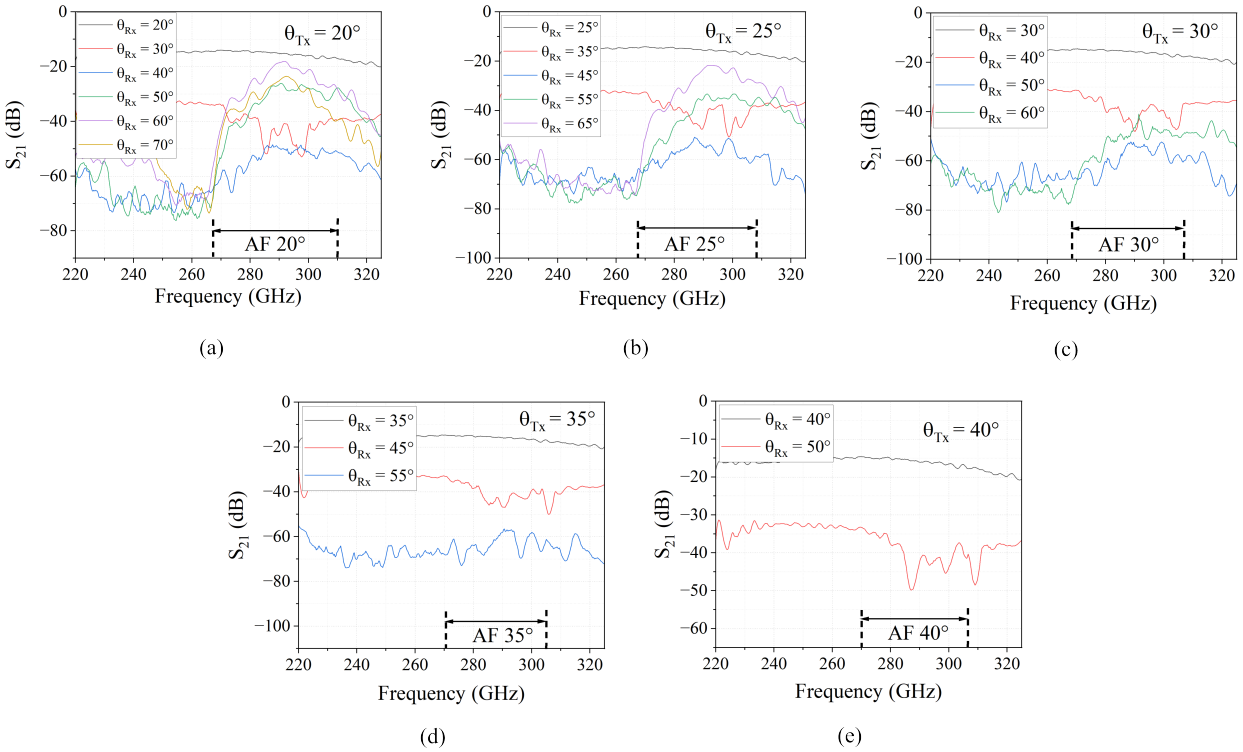

Fig. 10. Comparison between smoothed S_{21} for a metallic plate specular reflection (black) and nonspecular reflections from a RS (other colors) for (a) $\theta_{\mathrm{Tx}} = 20°$, (b) 25°, (c) 30°, (d) 35° and (e) 40°. The indicated RS bandwidth corresponds to the absorbed frequency (AF) range in the specular mode, see Fig. 8, this frequency being then non-specularly radiated from the RS.

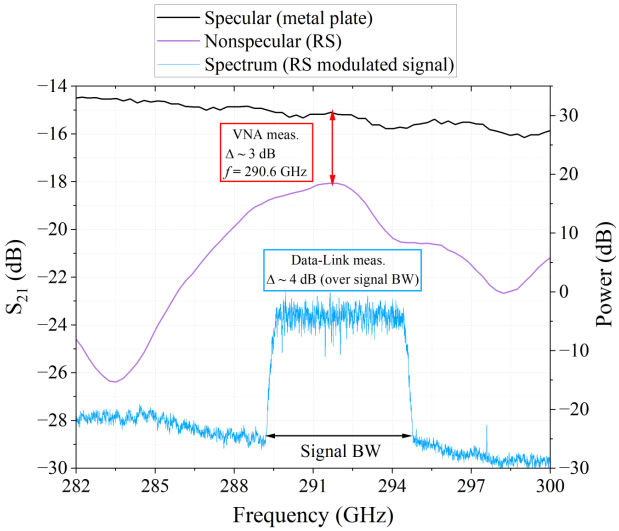

Fig. 11. Zoom on the smallest measured shift between smoothed specular reflection S_{21} from the metallic plate and the nonspecular reflection one from the RS which occur for $\theta_{\mathrm{Tx}} = 20°$ and $\theta_{\mathrm{Rx}} = 60°$. The reference spectrum (relative power in dB) of modulated THz data used to illuminate the RS in the last section, centered at 292 GHz.

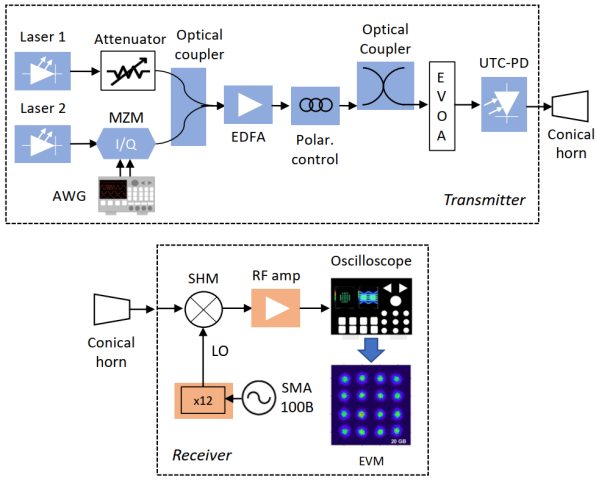

Fig. 12. Experimental setup of the insertion of the RS within the THz data-link. Transmitter and receiver placed in place of VNA ports 1 and 2 of Fig. II-H(b), respectively.

of the SHM (frequency dependence of the IF path in the SHM and IF amplifier gain) is corrected during equalization applied during the signal analysis. The SHM requires a LO tone around 150 GHz which is provided by a signal generator (SMA100B from Rohde & Schwarz) with a subsequent 12 multiplier. The IF signal is then first amplified (SHF 810 model from SHF) and captured by a 70 GHz real-time oscilloscope. This enables a real-time analysis of the usual performance metrics such as the error vector magnitude (EVM). The signal processing applied in the experiments is the following: first, typically short (below 1µs) scale time frames are sampled in order to limit the effect of the lasers phase noise on the IQ map. The local oscillator is adjusted to the center IF frequency at a value which is far from 0 Hz (typically

10.5 GHz) to enable a direct demodulation of the IQ signal using the commercial "digital demodulation" tool embedded in the Keysight Pathwave Vector Signal Analysis (89600 VSA software [43]), to compute the signals' EVM.

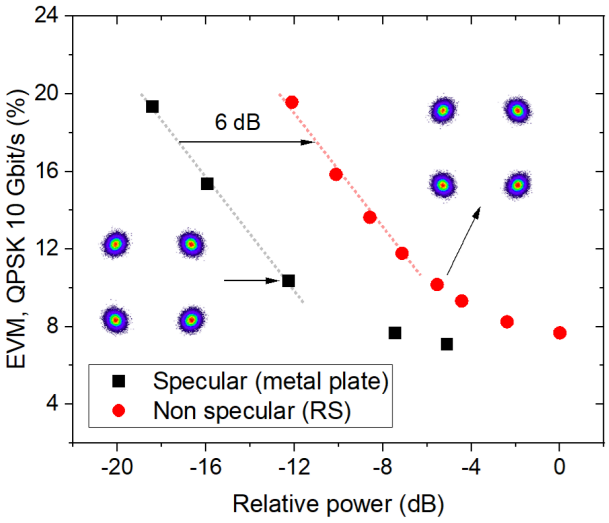

(a)

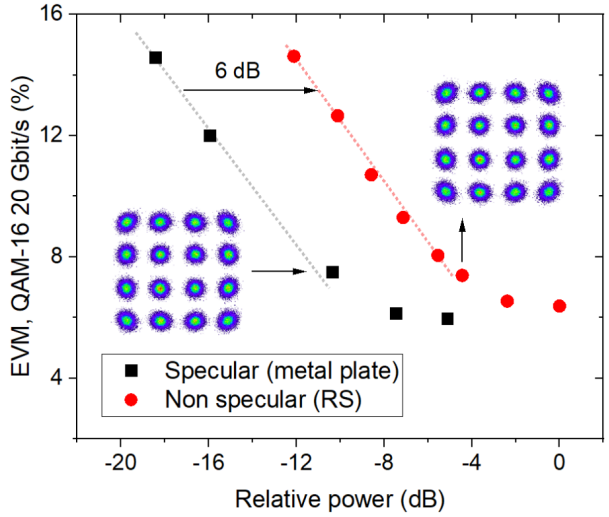

(b)

(a) EVMs for RS and metallic plate for (b) a QSPK modulation with a 10 GBits/s data rate and (c) a QAM-16 modulation with a 20 GBits/s data rate with carrier frequency of 292 GHz, together with the representative IQ constellation diagrams. Dotted lines are linear trend used to determine the power penalty, found to be about 6 dB in both cases.

B. RS performance evaluation

First, the system is optimized in terms of EVM in back-to-back (B2B), where transmit and receive circuits are directly waveguide connected to each other, using a 292 GHz carrier frequency. To be able to analyze the penalty induced by the RS in the OTA configuration, we compare the EVM performance of the link using the specular reflection on the metal plate and the case of nonspecular reflection on the RS. In both cases, the EVM is measured as function of the relative received power (power difference between B2B and OTA transmission), enabling to assess the power penalty (power shift to obtain the same EVM in each case) induced by the RS in the best angular configuration determined in the last section.

Fig. IV-A(b) and (c) shows the results for a QPSK and QAM-16 at 5 GBaud, for both specular cases (backside of the RS serving as metal plate) and nonspecular reflection on RS. We can clearly see that the behavior is very similar, shifted in the x-axis. The power penalty is found to be about 6 dB. Comparing with OTA measurements with VNA, as discussed before we could expect at least a 4 dB penalty. However, a higher penalty is obtained, but 4 dB estimation didn't consider some beam modifications or other specific effects due to the RS. In any case, this validates the insertion of the RS within the THz link, with a 6 dB penalty for NLoS THz link.

The determination of the losses associated to the RS operation in future THz links including reflective surfaces is a key point, as any loss has a direct impact in any communication scenario where the reflective surface is used. The measured power penalty induced by the use of the RS can be considered as an extra loss in the THz link budget and will have to be included in the design of NLoS THz links. The proposed method enables the determination of the RS penalty, which is a measured value in an over-the-air (OTA) case using a collimated beam. Such a value can then be inserted as a pure loss in the THz link budget as soon as the THz channel includes a non-specular reflection. Beyond this, depending on the RS type and especially if RS has beam shaping/focusing capabilities, the beam shape and gain-like effects could be included, but are beyond the scope of this study.

V. Conclusions and Outlook

An experimental characterization of the anomalous reflection using OTA measurements in the 300 GHz band is shown. This was carried out in two steps: first, a characterization by VNA method enabled to determine the RS specular absorption bandwidth. Then, a study of nonspecular reflections confirmed the RS operation, namely that depending on the difference between the angle of incidence and the angle of reflection, the absorption amplitude is modulated by the RS. At RS optimal point, the resulting signal obtained is deflected from specular reflection, with a $40°$ difference. It has then been shown that for the couple $(\theta_{\mathrm{Tx}}, \theta_{\mathrm{Rx}}) = (20°, 60°)$, the RS loss is minimal and is about 3 dB at 290.6 GHz. The RS was also successfully inserted in a real THz data-link, up to the EVM measurement of the RS relative to the metal plate. To the best of our knowledge, this is the first experimental demonstration of a THz data-link using complex modulated signal including a reflective surface.

References

[1] B. Zong, C. Fan, X. Wang, X. Duan, B. Wang and J. Wang, "6G Technologies: Key Drivers, Core Requirements, System Architectures,

and Enabling Technologies," in *IEEE Vehicular Technology Magazine*, vol. 14, no. 3, pp. 18-27, Sept. 2019, doi: https://doi.org/10.1109/MVT.2019.2921398.

[2] C. Han et al., "Terahertz Wireless Channels: A Holistic Survey on Measurement, Modeling, and Analysis," in *IEEE Communications Surveys & Tutorials*, vol. 24, no. 3, pp. 1670-1707, thirdquarter 2022, doi: https://doi.org/10.1109/COMST.2022.3182539.

[3] W. Jiang, B. Han, M. A. Habibi and H. D. Schotten, "The Road Towards 6G: A Comprehensive Survey," in *IEEE Open Journal of the Communications Society*, vol. 2, pp. 334-366, 2021, doi: https://doi.org/10.1109/OJCOMS.2021.3057679.

[4] C. D. Alwis et al., "Survey on 6G Frontiers: Trends, Applications, Requirements, Technologies and Future Research," in *IEEE Open Journal of the Communications Society*, vol. 2, pp. 836-886, 2021, doi: https://doi.org/10.1109/OJCOMS.2021.3071496.

[5] S. Basharat, M. Khan, M. Iqbal, U. S. Hashmi, S. A. R. Zaidi, I. Robertson, "Exploring reconfigurable intelligent surfaces for 6G: State-of-the-art and the road ahead." *IET Commun.* vol. 16(13), 1458-1474, 2022.

[6] C. A. Balanis, "Antenna theory: analysis and design". John Wiley & sons, 2016.

[7] Z. Chen, X. Ma, C. Han and Q. Wen, "Towards intelligent reflecting surface empowered 6G terahertz communications: A survey," in *China Communications*, vol. 18, no. 5, pp. 93-119, May 2021, doi: https://doi.org/10.23919/JCC.2021.05.007.

[8] ITU, "Attenuation by atmospheric gases and related effects", Report – P.676, Aug. 2022.

[9] ITU, "Specific attenuation model for rain for use in prediction methods", Report – P.838, Mar. 2005.

[10] J. M. Jornet and I. F. Akyildiz, "Channel Modeling and Capacity Analysis for Electromagnetic Wireless Nanonetworks in the Terahertz Band," in *IEEE Transactions on Wireless Communications*, vol. 10, no. 10, pp. 3211-3221, October 2011, doi: https://doi.org/10.1109/TWC.2011.081011.100545.

[11] T. Kürner et al., "THz Communications and the Demonstration in the ThoR–Backhaul Link," in *IEEE Transactions on Terahertz Science and Technology*, vol. 14, no. 5, pp. 554-567, Sept. 2024, doi: https://doi.org/10.1109/TTHZ.2024.3415480.

[12] A. Renau et al., "300 GHz super heterodyne link over 645 m with frequency duplexing for point to point backhauls," 2023 *53rd European Microwave Conference (EuMC)*, Berlin, Germany, 2023, pp. 130-133, doi: https://doi.org/10.23919/EuMC58039.2023.10290501.

[13] F. Yang, P. Pitchappa, N. Wang, "Terahertz Reconfigurable Intelligent Surfaces (RISs) for 6G Communication Links". *Micromachines* 2022, 13, 285, doi: https://doi.org/10.3390/mi13020285.

[14] Z. Shen, W. Li, B. Jin and D. Zhao, "A liquid crystal-based multi-bit terahertz reconfigurable intelligent surface," in *APL Photon.*, vol. 3, 016109, 2024, doi: https://doi.org/10.1063/5.0176272.

[15] Z. Chen, B. Ning, C. Han, Z. Tian and S. Li, "Intelligent Reflecting Surface Assisted Terahertz Communications Toward 6G," in *IEEE Wireless Communications*, vol. 28, no. 6, pp. 110-117, December 2021, doi: https://doi.org/10.1109/MWC.001.2100215.

[16] M. Jian et al., "Reconfigurable intelligent surfaces for wireless communications: Overview of hardware designs, channel models, and estimation techniques," in *Intelligent and Converged Networks*, vol. 3, no. 1, pp. 1-32, March 2022.

[17] Y. Liu et al., "Reconfigurable Intelligent Surfaces: Principles and Opportunities," in *IEEE Communications Surveys & Tutorials*, vol. 23, no. 3, pp. 1546-1577, thirdquarter 2021, doi: https://doi.org/10.1109/COMST.2021.3077737.

[18] E. Björnson, Ö. Özdogan, and E. G. Larsson, "Reconfigurable Intelligent Surfaces: Three Myths and Two Critical Questions," in *IEEE Communications Magazine*, vol. 58, no. 12, pp. 90-96, December 2020, doi: https://doi.org/10.1109/MCOM.001.2000407.

[19] E. Basar, M. Di Renzo, J. De Rosny, M. Debbah, M. -S. Alouini and R. Zhang, "Wireless Communications Through Reconfigurable Intelligent Surfaces," in *IEEE Access*, vol. 7, pp. 116753-116773, 2019, doi: https://doi.org/10.1109/ACCESS.2019.2935192.

[20] C. Huang, A. Zappone, G. C. Alexandropoulos, M. Debbah and C. Yuen, "Reconfigurable Intelligent Surfaces for Energy Efficiency in Wireless Communication," in *IEEE Transactions on Wireless Communications*, vol. 18, no. 8, pp. 4157-4170, Aug. 2019, doi: https://doi.org/10.1109/TWC.2019.2922609.

[21] E. C. Strinati et al., "Reconfigurable, Intelligent, and Sustainable Wireless Environments for 6G Smart Connectivity," in *IEEE Communications Magazine*, vol. 59, no. 10, pp. 99-105, October 2021, doi: https://doi.org/10.1109/MCOM.001.2100070.

[22] H. Zhang, B. Di, K. Bian, Z. Han, H. V. Poor and L. Song, "Toward Ubiquitous Sensing and Localization With Reconfigurable Intelligent Surfaces," in *Proceedings of the IEEE*, vol. 110, no. 9, pp. 1401-1422, Sept. 2022, doi: https://doi.org/10.1109/JPROC.2022.3169771.

[23] H. Wymeersch, J. He, B. Denis, A. Clemente and M. Juntti, "Radio Localization and Mapping With Reconfigurable Intelligent Surfaces: Challenges, Opportunities, and Research Directions," in *IEEE Vehicular Technology Magazine*, vol. 15, no. 4, pp. 52-61, Dec. 2020, doi: https://doi.org/10.1109/MVT.2020.3023682.

[24] P. del Hougne, 'Robust position sensing with wave fingerprints in dynamic complex propagation environments', Physical Review Research, vol. 2, p. 043224, Nov. 2020.

[25] I. Alamzadeh, G. C. Alexandropoulos, and M. F. Imani, "Intensity-only OMP-based direction estimation for hybrid reconfigurable intelligent surfaces," *IEEE International Symposium on Antennas and Propagation and USNC-URSI Radio Science Meeting*, Portland, USA, 23–28 July 2023.

[26] D. Demmer, F. F. Manzillo, S. Gharbieh, M. Śmierzchalski, R. D'Errico, J.-B. Doré, and A. Clemente. 2023. "Hybrid Precoding Applied to Multi-Beam Transmitting Reconfigurable Intelligent Surfaces (T-RIS)" Electronics 12, no. 5: 1162.

[27] N. Shlezinger, G. C. Alexandropoulos, M. F. Imani, Y. C. Eldar and D. R. Smith, "Dynamic Metasurface Antennas for 6G Extreme Massive MIMO Communications," in *IEEE Wireless Communications*, vol. 28, no. 2, pp. 106-113, April 2021, doi: https://doi.org/10.1109/MWC.001.2000267.

[28] I. Alamzadeh, G. C. Alexandropoulos, N. Shlezinger, and M. F. Imani, "A reconfigurable intelligent surface with integrated sensing capability," Nature Scientific Reports, vol. 11, no. 20737, pp. 1–10, Oct. 2021.

[29] Y. Liu et al., "STAR: Simultaneous Transmission and Reflection for 360° Coverage by Intelligent Surfaces," in *IEEE Wireless Communications*, vol. 28, no. 6, pp. 102-109, December 2021, doi: https://doi.org/10.1109/MWC.001.2100191.

[30] ETSI white paper, "Reconfigurable Intelligent Surfaces (RIS); Use Cases, Deployment Scenarios and Requirements," – ETSI GR RIS 001, Apr. 2023.

[31] S. Abadal, T.-J. Cui, T. Low and J. Georgiou, "Programmable Metamaterials for Software-Defined Electromagnetic Control: Circuits, Systems, and Architectures," in *IEEE Journal on Emerging and Selected Topics in Circuits and Systems*, vol. 10, no. 1, pp. 6-19, March 2020, doi: https://doi.org/10.1109/JETCAS.2020.2976165.

[32] Z. Zhang et al., "Active RIS vs. Passive RIS: Which Will Prevail in 6G?," in *IEEE Transactions on Communications*, vol. 71, no. 3, pp. 1707-1725, March 2023, doi: https://doi.org/10.1109/TCOMM.2022.3231893.

[33] K. T. Selvan and R. Janaswamy, "Fraunhofer and Fresnel Distances: Unified derivation for aperture antennas," in *IEEE Antennas and Propagation Magazine*, vol. 59, no. 4, pp. 12-15, Aug. 2017, doi: https://doi.org/10.1109/MAP.2017.2706648.

[34] Q. Gu, D. Wu, X. Su, J. Jin, Y.Yuan, J. Wang, "Performance Comparisons between Reconfigurable Intelligent Surface and Full/Half-duplex Relays," *2021 IEEE 94th Vehicular Technology Conference (VTC2021-Full)*, Norman, OK, USA, 2021, pp. 01-06.

[35] S. K. Singh, K. Agrawal, K. Singh, B. Clerckx, C.-P. Li, "RSMA for Hybrid RIS-UAV-Aided Full Duplex Communications with Finite Blocklength Codes Under Imperfect SIC," in *IEEE Transactions on Wireless Communications*, vol. 22, no. 9, pp. 5957-5975, 2023.

[36] E. Björnson and L. Sanguinetti, "Power Scaling Laws and Near-Field Behaviors of Massive MIMO and Intelligent Reflecting Surfaces," in *IEEE Open Journal of the Communications Society*, vol. 1, pp. 1306-1324, 2020, doi: https://doi.org/10.1109/OJCOMS.2020.3020925.

[37] S. Zeng *et al.*, "RIS-based IMT-2030 Testbed for MmWave Multi-Stream Ultra-Massive MIMO Communications", in *IEEE Wireless Communications*, vol. 31, no. 3, pp. 375-382, 2024.

[38] N. Yu, P. Genevet, M. A. Kats, F. Aieta, J.-P. Tetienne, F. Capasso and Z. Gaburro, "Light Propagation with Phase Discontinuities: Generalized Laws of Reflection and Refraction." *Science* **334**, 6054 (2011).

[39] A. Díaz-Rubio, V. S. Asadchy, A. Elsakka, S. A. Tretyakov, "From the generalized reflection law to the realization of perfect anomalous reflectors." *Science Advances*, vol. 3, no. 8), e1602714, 2017.

[40] A. K. Battacharyya, "Phased Array Antennas: Floquet Analysis, Synthesis, BFNs, and Active Array Systems". John Wiley & sons, 2005.

[41] S. K. R. Vuyyuru, L. Hao, M. Rupp, S. A. Tretyakov, R. Valkonen, "Modeling RIS from Electromagnetic Principles to Communication Systems–Part I: Synthesis and Characterization of a Scalable Anomalous Reflector," *arXiv preprint arXiv:2403.12790v1*, 2024.

[42] https://vadiodes.com/en/

[43] https://www.keysight.com/us/en/products/software/pathwave-test-software/89600-vsa-software.html

VI. Biography Section

Frédéric Dutin received the Ph.D. degree in Laser Physics from the LOMA (Laboratoire Ondes et Matière d'Aquitaine), Talence, France in 2020. From 2021 to 2022, he held a post-doctoral position in laser-plasma interaction with the LOA (Laboratoire d'Optique Appliquée), Palaiseau, France. He is currently holding a post-doctoral position with the IEMN (Institut d'Electronique, de Microélectronique et de Nanotechnologie), Villeneuve d'Ascq, France. His current research interests include THz time domain spectroscopy, metasurface, reconfigurable elements, manipulation of the wave propagation and optical communications for THz applications.

Unai Beaskoetxea received the Ph.D. degree in telecommunication engineering from the Public University of Navarra (UPNA), Pamplona, Spain, in 2017. From 2013 to 2019 he worked as a researcher at the Antenna Group, UPNA; as a visiting researcher at Queen Mary University London, London, UK; and at Università degli Studi di Siena, Siena, Italy. He has published 7 papers in international journals, more than 10 national and international conferences, and contributed to a book chapter. From 2019 and 2024, he worked as a researcher engineering at Anteral S.L., Pamplona, Spain. His current research interests are high-frequency antennas and frequency selective surfaces.

Victor Torres received the Ph.D. degree in telecommunication engineering from the Public University of Navarra (UPNA), Pamplona, Spain, in 2014. He pursued his academic research career between 2010 and 2016 at the Antenna Group, UPNA; at the University of Pennsylvania, Philadelphia, USA; at Imperial College London, London, UK; and at the Nanophotonics Technology Center, Valencia, Spain. In 2016, he joined Anteral S.L., Pamplona, Spain, as a THz Engineer, and since 2019, he has served as CTO of Radar Technology. He has published 18 international journal papers, contributed to over 80 national and international conference papers, and has been actively involved in more than 20 European and regional research projects. His current research interests focus on metamaterials, antennas and radar technology at millimeter and terahertz frequencies. As Anteral's CTO, he develops high-performance antennas, passive components, radar products and technologies in the microwave, millimeter, submillimeter, and THz frequency bands.

Pascal Szriftgiser received the Ph.D. degree in quantum physics from the Laboratoire Kastler Brossel, University Paris VI (Sorbonne University today), Paris, France (1996). The same year, as a researcher, he joined CNRS (Centre National de la Recherche Scientifique) at Laboratory PhLAM (Physique des Lasers Atomes et Molécules). Since 2012, he is a CNRS Research Director. From 2014 to 2021, he was the Leader of the Cold Atoms Group and Deputy Director of the Laboratory PhLAM from 2019 to 2021. Since 2021, he currently is PI of Contrat de Projet Etat Région (CPER) WaveTech@HdF, a consortium that brings together six research laboratories in Hauts-de-France region. He has authored or co-authored 140 publications in peer-reviewed international journals or conference proceedings. His expertise spans from cold atoms physics, quantum chaos, topology, and nonlinear optics in optical fibers to high-speed coherent optical communications for THz applications.

Jorge Teniente received the Ph.D. degree in telecommunication engineering from the Public University of Navarra (UPNA), Pamplona, Spain, in 2003. Since 1997, he has been with the Antenna Group, UPNA, where he is currently an Associate Professor. From 1999 to 2000, he was a Spanish Trainee at European Space Agency (ESA)/ESTEC, Noordwijk, The Netherlands. In Summer 2002, he was a Research Scientist at the ESA Project "Star-Tiger 1," Rutherford Appleton Laboratory, Chilton, Didcot, U.K., and from 2004 to 2005, he was at the University of Oviedo, Asturias, Spain. During his research activity, he has been actively involved in 128 research projects, including 52 public projects and 76 contracts with companies, 61 of which he directed. He has authored 33 articles in scientific journals, with nine of them as the first author. Additionally, he contributed to three book chapters and presented 127 papers at various scientific conferences, comprising 52 national and 75 international conferences. He is also a founding partner of the company Anteral S.L., Pamplona, Navarra. His current area of research is in the field of horn antenna technology, orthomode transducers (OMTs), septums and polarizers and in design, manufacture and measurement of horn antennas in mm-wave, sub-mm-wave, and THz frequencies as well as fabrication of mm and submm-wave circuits at clean room environment.

Guillaume Ducournau is with the Institute of Electronics, Microelectronics and Nanotechnology (IEMN), UMR-CNRS 8520, University of Lille, Villeneuve d'Ascq, France, since 2007. He is the Leader of the THz wireless communications activity with IEMN using optoelectronic THz photomixers, electronic receivers, THz instrumentation, and millimeter-wave (mm-wave) characterization. He worked on several European projects: STREP ROOTHz 2010-2013, ThoR H2020, GRAPH-X, TIMES (6G SNS) as well as the Marie-Skłodowska Curie TERAOPTICS network. At national level he was the Coordinator of the COM'TONIQ Project from 2014 to 2017 funded by ANR (INFRA 2013) dedicated to THz communications in the 300 GHz band, the ANR/DFG TERASONIC project for the use of THz photonics technologies and electrical solid-state technologies for THz communications and SPATIOTERA for spatially-distributed photomixers. He received the 2020 ISAP BEST PAPER award. He is involved in national France 2030 programs gathering several French laboratories under the 'PEPR' programs funded by the ANR (Agence Nationale de la Recherche). In this framework, the FUNTERA project (6 partners) is investigating THz converters, while the SYSTERA project (12 partners) is dedicated to beyond 90 GHz systems for future networks. He also participates to the ST-IEMN common laboratory, and more specifically involved in the mm-wave technologies characterization part. He has authored or co-authored more than 180 publications in peer-reviewed international journals or peer-reviewed conferences proceedings and holds 1 patent.